*Egyptian Geophysical Society*
*EGS Journal, Vol. 13, No. 1, 83-102 (2015)*

# JOINT INVERSION OF TRANSIENT ELECTROMAGNETIC AND DC-RESISTIVITY SOUNDING DATA FOR IMAGING PERCHED WATER OCCURRENCES AT THE BEDOUIN VILLAGE 'FUKA', NORTHWESTERN MEDITERRANEAN COAST OF EGYPT

K.S.I. Farag[(1)] and B. Tezkan[(2)]

[(1)] *Geophysics Department, Faculty of Science, Ain Shams University, Abbassia 11566, Cairo, Egypt.*

[(2)] *Institut fur Geophysik und Meteorologie, Universitaet zu Koeln, Albertus-Magnus-Platz, D-50923 Koeln, Germany.*

## النمذجة العكسية المشتركة لبيانات طرق السبر الكهرومغناطيسية الوقتية والمقاومة النوعية –ذات التيار الثابت– لتصوير تواجدات المياه الأرضية الجاثمة بقرية 'فوكه' البدوية بالساحل الشمالى الغربى البحرمتوسطى لمصر

**الخلاصة:** تمثل قرية 'فوكه' البدوية شريطاً ضيقاً على طول الطريق الساحلى السريع الإسكندرية – مرسى مطروح، ما يقرب من ٢٢٥ كم من مدينة الإسكندرية وحوالى ٦٥ كم من مدينة مرسى مطروح. وتتمركز القرية عند خط عرض ٣١ درجة ٠٤ دقيقة ٣٠ ثانية شمالاً وخط طول ٢٧ درجة ٥٥ دقيقة ٤٥ ثانية شرقاً، وتبلغ مساحتها نحو٢٥ كم٢. وتعد ضمن المناطق التنموية الأكثر جذباً بمحافظة مطروح. يستمد هذا الجذب من توافر موارد إستراتيجية لمياه أرضية جاثمة ضحلة بالقرية ومن الكثافة السكانية المنخفضة نسبياً بها، فضلاً عن الإمكانات الطبيعية المتاحة للسياحة فى المستقبل القريب. الوضع الهيدروجيولوجى لحوض قرية "فوكه" مرتبط تماما بالعلاقة بين الجيومورفولوجية الإقليمية للحوض والتراكيب الجيولوجية التحتسطحية والظروف المناخية البحرمتوسطية الجافة/شبه الجافة. تم تنفيذ ما مجموعه ٣٢ جسة (سبر) رأسية ذات موقع مشترك لطريقتى الكهرومغناطيسية الوقتية المتمركزة والمقاومة النوعية –ذات التيار الثابت– على طول ٧ مسارات سطحية للقياسات. الأهداف الرئيسية تتمثل فى تصوير وتمييز طبقات المياه الأرضية الجاثمة الضحلة عن تواجدات المياه المتوسطة/العميقة. وبمتابعة عرض البيانات وإجراء التحويلات الأولية لها، تم تفسير تلك البيانات على نطاق واسع ومتسق، سواء بشكل منفرد أو مشترك، فى شكل نماذج عكسية أحادية البعد للمقاومة الكهربائية المتدرجة على طول المسارات السطحية للقياسات. وبغض النظر عن التشابه القريب بين الوحدات الجيوكهربائية المستنتجة من بيانات الطريقتين، عند نمذجة البيانات عكسياً بشكل منفرد، كانت لا تزال المضاهاة بين تلك الواحدات غير مرضية. حيث أكد التحليل الخطى المتعادل أن كلاً من الطبقات شديدة الإرتفاع فى المقاومة النوعية والمنمذجة عكسياً لبيانات طريقة الكهرومغناطيسية الوقتية المتمركزة والطبقات شديدة الإنخفاض فى المقاومة النوعية والمنمذجة عكسياً لبيانات طريقة المقاومة النوعية –ذات التيار الثابت– تظهر إلى حد ما سميكة جداً، و قد تبدو أعلى تحديداً. هذا ولقد تحقق تحسن كبير فى الوضوح التحتسطحى لتراكيب المقاومة النوعية الضحلة منها أوالعميقة عند نمذجة البيانات عكسياً بشكل مشترك حيث قلت الأخطاء المحيطة للطبقات شديدة الارتفاع أو الانخفاض فى المقاومة النوعية بشكل ملحوظ. هذا وقد أبرز المسح الميداني الحالى مدى التطبيق والكفاءة والدقة فى إستخدام كل من طرق السبر الكهرومغناطيسية الوقتية والمقاومة النوعية –ذات التيار الثابت– بشكل مشترك، عن أى إستخدام منفرد، لتصوير وتمييز أفضل لطبقات المياه الأرضية الجاثمة الضحلة الإستراتيجية عن تواجدات المياه المتوسطة/العميقة على طول الساحل الشمالى الغربى البحرمتوسطى لمصر.

**ABSTRACT:** *The Bedouin village 'Fuka' represents a narrow strip along the Alexandria–Marsa Matrouh coastal highway, approximately 225 km from Alexandria and 65 km from Marsa Matrouh. It is roughly centered at latitude 31$^o$ 04' 30" N and longitude 27$^o$ 55' 45" E, and has an area of some 25 km$^2$. It is among the most attractive development areas in Matrouh Governorate. This attraction is derived from the strategic shallow perched water resources available in the village and relatively low population density, as well as the available natural potentials for near-future tourism. The hydrogeological setting in Fuka basin is highly controlled by the relationship between its regional geomorphology, subsurface geological structures and semi-arid/arid Mediterranean climatic conditions. A total of 32 co-located vertical central in-loop transient electromagnetic (CINL–TEM) and Schlumberger DC–resistivity (DCR) soundings along 7 surveying traverses were conducted. Main objectives were to image and differentiate the shallow perched water-bearing layers from the whole intermediate/deep groundwater occurrences. Following up data viewing and preliminary transformations data were extensively and consistently interpreted, both individually or jointly, in terms of one-dimensional (1D) inverted electrical resistivity smoothed-models along the surveying traverses. Apart from the close resemblance between the encountered CINL–TEM and DCR geoelectric units, when inverting both data sets individually, they are still clearly showing an unsatisfied correlation. Linear equivalence analysis showed that both the individually-inverted CINL–TEM highly-resistive and DCR highly-conductive layers appeared somewhat too thick, and seemed to be relatively overdetermined. A significant resolution improvement for both the shallow and deep resistivity structures has been achieved when inverting both data sets jointly. The layer bounding errors for both the jointly-inverted CINL–TEM highly-resistive and DCR highly-conductive layers were impressively decreased. Finally, the present field survey highlighted the applicability, efficiency and reliability of utilizing both the CINL–TEM and DCR sounding methods, than any individual use, for better imaging and differentiating the strategic shallow perched water-bearing layers from the whole intermediate/deep groundwater occurrences along the Northwestern Mediterranean coastal plain of Egypt.*

## 1. INTRODUCTION

Numerous studies have demonstrated that the joint one-dimensional (1D) smoothed-earth inversion of multiple galvanic–inductive data, where a single model satisfies those data sets, will generally enhance the resolution of the subsurface resistivity distribution (Jupp and Vozoff, 1975; Raiche et al., 1985; Hohmann and Raiche, 1988; Sandberg, 1993; Albouy et al., 2001). Thus, joining of these data sets must be expected to drastically reduce ambiguity problems with layer equivalence and suppression, which are otherwise encountered within each individual data set independently.

Preferred, but not necessary, conditions for such measured data sets are; to be co-located in the field (like the centred transient electromagnetic (TEM) and DC–resistivity (DCR) soundings), to have an identical operative physical property (like electrical resistivity), to employ the same field-of-source (like DC-current), to have a comparative depth-of-investigation (which can be easily obtained by controlling TEM transmitter moment and maximum DCR current-electrode half-spacing to an equivalent degree), and to have interchangeable resolution capabilities (where the inductive TEM methods are only sensitive to the conductive subsurface media and the galvanic DCR methods are only sensitive to the resistive subsurface media within the earth model). So, the related TEM and DCR sounding data sets can be regarded as ideal partners with complementary characters for further joint inversion.

To determine how well the smoothed-earth model fits the measured data at each sounding, the usual weighted least-squares criterion (root-mean-square (RMS) misfit) is usually used, attempting generally at minimizing the familiar difference estimates. Applying the standard resolution/sensitivity statistics (e.g., linear equivalence analysis), by inspecting the bounding errors of the inverted layer parameters (layer thicknesses or electrical resistivities) (Jackson, 1972; Jupp and Vozoff, 1975 and Goldman et al., 1994; Meju, 1994), typically for the best-fitted resistivity model at each sounding, is very important as they show quantitatively how much confidence can be placed in that model.

Ground-based TEM sounding methods can be used in a number of different transmitter–receiver configurations (Nabighian and Macnae, 1991) for routine hydrogeological investigations. Among these different loop-loop configurations, the central in-loop (CINL) configuration has become more popular and is presently in wide use. On the other hand, the conventional DCR sounding methods, in the form of Schlumberger or Wenner configurations, have proven to be effective in such applications.

## 2. TRANSIENT ELECTROMAGNETIC (TEM) SOUNDING METHODS

### 2.1 Conceptual Background

TEM sounding methods utilize EM energy introduced into the ground as transient pulses, instead of continuous waves, by a large transmitter-loop carrying steady current and primary magnetic field. Satisfying Faraday's law, immediately after the current and primary field are suddenly turned-off, an associated secondary magnetic field resulting from an induced current pattern in the ground is sensed by a centrally-placed small receiver-loop and decays with time as the current gradually dissipates. The configuration forms the basis of the central in-loop (CINL–TEM) sounding and can be schematically demonstrated in Fig. 1. The spreading out of induction currents is much like the downward movement of a system of smoke rings (Nabighian, 1979; Oristaglio and Hohmann, 1984; Nabighian and Macnae, 1991; West and Macnae, 1991), which have a consequential amplitude decay with increasing time. These current rings are snapshots in time through a vertical section in the ground and can move outwards once they reach a layer interface with a sufficient resistivity-contrast.

Initially, the induced currents are concentrated close to the ground surface, just below the transmitter-loop, and dissipated through ohmic losses. This is known as the early-time stage, where the secondary magnetic field is time-invariant and weakly-dependent on the near-surface resistivity. Effectively, this is the start of downward diffusion of the current system towards the ground interior, approaching the intermediate-time stage. As time passes and the locus of maximum current amplitude diffuses downwards, the secondary field becomes time-variant and proportional to $t^{-5/2}$ and to $\rho^{-3/2}$, where t is the decay time after current turn-off [Sec.] and $\rho$ is the deep-ground resistivity [Ohm.m]. This is known as the late-time stage. Generally, the magnetic field decays rapidly when the currents diffuse in a resistive ground, and more slowly when they flow in a conductive ground. The recorded signal is either a decay of the vertical secondary magnetic field component (step response) or its time-derivative (impulse response or voltage), and generally called a transient. Magnetic field measurements are usually superior only in penetrating conductive ground, while voltage measurements are suitable for both conductive and fairly resistive grounds. Only the latter will be considered here.

Now consider a fairly conductive homogeneous half-space or an uniform horizontally-layered earth with geometry applicable to many opencast mining problems. According to Ward and Hohmann (1988), the CINL–TEM voltage response is given by

$$\frac{\partial h_z}{\partial t} = \frac{-I\rho}{\mu_0 a^3}\left[3erf(\theta a) - \frac{2\theta a}{\sqrt{\pi}}(3 + 2\theta^2 a^2)e^{-\theta^2 a^2}\right],$$

where $I$ is the transmitter current [A], $\theta=(\mu_o/\rho 4t)^{1/2}$, $a$ is the transmitter-loop radius [m] and $erf(\theta a)$ is the error function

$$erf(\theta a) = \frac{2}{\sqrt{\pi}} \int_0^{\theta a} e^{-t^2} dt \, .$$

At later times, the mathematics simplifies the definition considerably and the relevant asymptotic formula can be given as

$$\frac{\partial h_z}{\partial t} \approx \frac{-I \mu_o^{3/2} a^2}{20 \pi^{1/2} \rho^{3/2} t^{5/2}} .$$

Commonly, CINL–TEM data are presented in the form of bilogarithmic plot of transient-decay response versus time (Fig. 8). Although the rate and spatial characteristics of this decay are dependent on the ground resistivity-distribution (Nabighian, 1979), they are not directly representative of the resistivity structure at the sounding location. To make the curve more representative, the transient-decay response should be transformed into apparent resistivity.

## 2.2 Depth-of-Investigation (DOI)

Analogous to frequency-domain EM (FDEM) methods, defining a depth-of-investigation is crucial for CINL–TEM methods. Theoretically, the penetration depth at which the induced currents still strongly diffuse, and therefore the response due to a buried homogeneous half-space can be detected by a CINL–TEM system at a particular sampling time, is known as diffusion-depth [m] (Spies, 1989)

$$\delta_{TEM} = \sqrt{\frac{2t\rho_a}{\mu_o}} \, .$$

The similarity between the FDEM skin-depth and CINL–TEM diffusion-depth is remarkable: the skin-depth is proportional to $(1/f)^{1/2}$, whereas the diffusion-depth is proportional to $t^{1/2}$. Where $f$ is the operating frequency. So, it is to CINL–TEM methods what the skin-depth is to FDEM methods. Furthermore, it is apparently independent of the configuration size and geometry. In practice, the effective depth-of-investigation is dependent not only on the weighted-average ground resistivity and sampling time, but also on the transmitter-dipole moment (the effective area times output-current) $M$ and the overall signal-to-noise ratio (SNR), and hence the sensitivity and accuracy of the instrumentation. For conventional near-zone CINL–TEM soundings, in which the transmitter-loop size is less than the excepted depth-of-investigation, it can be given as

$$d_{TEM} \approx 0.55 \left[ \frac{M \rho_a}{\eta_v} \right]^{1/5},$$

where $\eta_v$ the background noise level [typically 0.1 nV/Am$^2$]. That means, it is more difficult to sound more deeply unless the transmitter-dipole moment is effectively large and the signal is sufficiently strong with respect to the background noise. Generally, the earliest sampling time determines the minimum depth-of-investigation at which near-surface resistivity variations can be reasonably resolved, and vice versa.

## 2.3 Zonge® NanoTEM Measuring System

The present CINL–TEM data were collected using the commercially available NanoTEM system (Zonge Engineering and Research Organization Inc., USA) along 7 surveying traverses, comprising a total of 32 soundings (Fig. 3, lower). It is a single-site acquisition system that offers a high-resolution imaging of the shallow and sufficiently-deep resistivity structures. When the standard CINL configuration is used (Fig. 1), a single-turn 50 x 50 m$^2$ transmitter-loop is laid out on the ground and connected to the battery-powered 'NT–20' transmitter. Tall wooden sticks are usually pushed into the ground at the corners of the transmitter-loop to provide sighting targets. A single-turn 20 x 20 m$^2$ receiver-loop is located at the center of the transmitter-loop, by sighting on the corner sticks with the right-angle prism, and connected to the 'GDP–32II' receiver as pictured in Fig. 2 (left). The instrumental resolution is limited around 0.05 μV. Data acquisition parameters and specifications of the NanoTEM system are given in Table 1.

***Table (1): Summary of data acquisition parameters and specifications used in the Zonge NanoTEM measuring system.***

| **Acquisition Parameter** | **NanoTEM Measuring Mode** |
|---|---|
| **Configuration** geometry | Central in-loop (CINL) |
| **Transmitter** ($T_X$) | |
| Area [m$^2$] | 50 × 50 |
| Type | 12/24 V battery-powered 'NT–20' |
| Current output [A] | 0.5 (low gain) to 3 (high gain) |
| Number-of-turns | Zero-elevated single turn |
| Waveform and duty cycle | Square bipolar current with 50% duty cycle* |
| Turn-off (ramp) time [μs] | 3 |
| **Receiver** ($R_X$) | |
| Area [m$^2$] | 20×20 |
| Type | Multi-channel 'GDP–32II'** |
| Number-of-turns | Zero-elevated single turn |
| Measured component(s) | $(\partial h_z/\partial t)$*** as voltage decay |
| Time gates (windows) | 31 gates covering approximately four decades at earlier-times |
| Band-width (repetition rate) [Hz] | 64 |
| Sampling rate (window centres) [μs] | Manually set at 1.6 |
| Gain-setting | Manual low and high gain |
| Number-of-cycles to be averaged | 1024 |
| Number-of-stacks | 10 |
| Dumped data file | A 31 data-point binary file, easily transformed into ASCII text format |

*50% of a constant period between successive cycles in which the transmitter current is delivered during a complete cycle (two signals of the same shape and polarity). **Multi-functional geophysical data processor, model 32II. ***Other magnetic-field components, using a multiple receiver-loop system, are recently possible (e.g. Helwig et al., 2004).

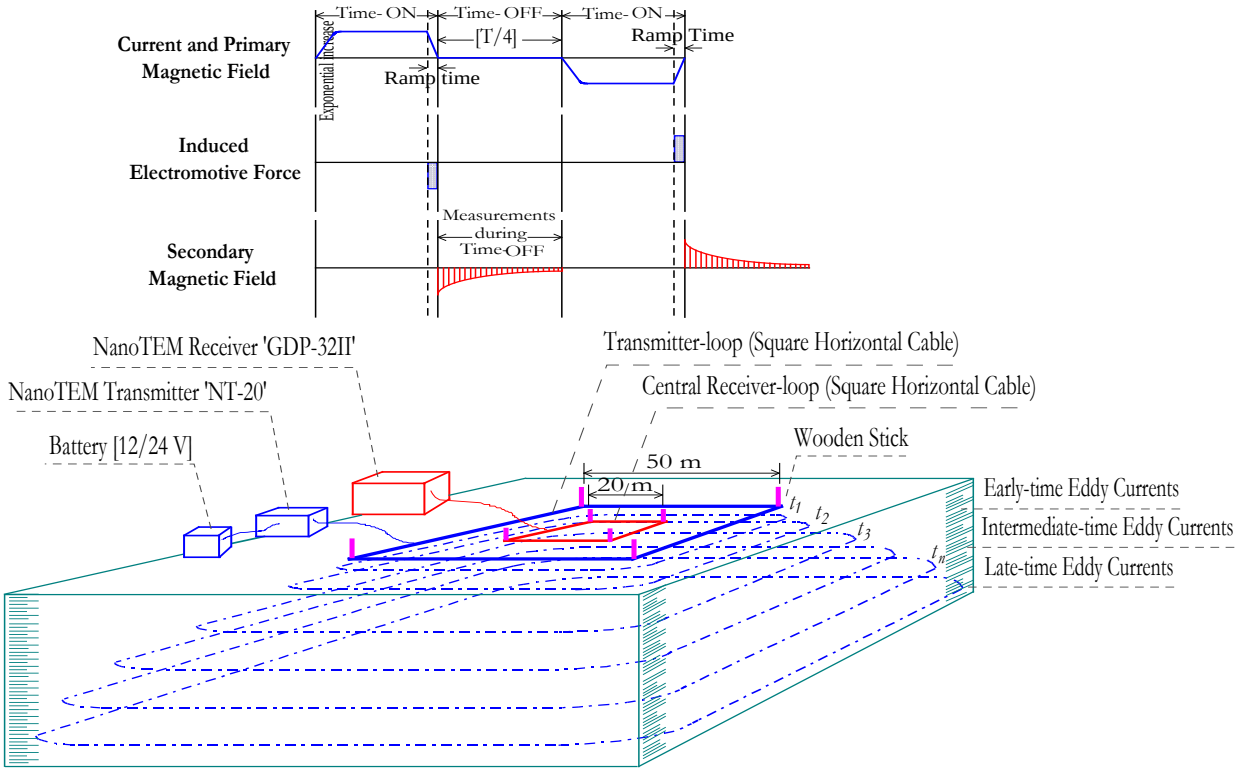


**Fig. (1): Central in-loop field setup of the Zonge® NanoTEM measuring system (Farag, 2005). The downward and outward propagation of the eddy currents at successive time intervals over a homogeneous ground are displayed. In the upper part, the bipolar transmitter-current waveform, induced electromotive force in the receiver-loop, and secondary magnetic field measured during the time-off are illustrated.**


**Fig. (2): Photographs showing both (left) the Zonge® NanoTEM and (right) ABEM™ Terrameter SAS–1000 measuring systems and other connections in the field.**

The 'GDP-32II' applies a scheme of synchronous filtering, including anti-alias, digital powerline-notch and telluric filters, as well as self-potential (SP) buckout, to reject most of the broad-band natural EM and cultural noise. Furthermore, it sets a number of discrete time-windows, or gates, of finite width to measure the transient-decay amplitude after the applied current is turned-off. These gates are arranged logarithmically and controlled by changing the selected bandwidth. Normally, the transient-decay response changes rapidly at early times and more slowly at later times. To minimize the amplitude distortion, the early-time gates are set very narrow, later-time gates are set much wider (Zonge Engineering and Research Organization Inc., 2000). Windowing is desirable since wider gates enhance the SNR at later-times.

Signals due to a positive pulse and the next negative pulse are then averaged, and considered to be one cycle. Signals can be averaged over as many as 1024 cycles to obtain an output-average for each gate.

This is performed simultaneously over all gates so that the background noise is common to all gates at the time of measurement. Transient-decay data are stacked (statistically averaged) online to reduce the data quantity to a manageable size and to enhance the overall SNR. The standard deviations derived from the extensive stacking are usually used as weights in all inversion schemes. The acquisition software easily permits the data sets to be sampled, self-checked while recording and stored as time series in a solid-state memory. All data are in a block format and can be transferred digitally to any MS DOS-based PC via a serial interface. No further data processing is done in the field. Finally, the measured transients are automatically normalized at each sampling time from the output-current, to be given in units of V/A.

In this recording fashion, the system has sufficiently early- to late-time information to be able to capture adequate TEM signals and to suppress instrumental and background noise problems. Sufficient early-time measurements usually result in a better resolution of shallow resistivity structures, and can be a determining factor in reducing the ambiguity caused by model equivalence in interpretation of geoelectric parameters for sufficiently-deep resistivity structures (Goldman et al., 1994). The ambient/background electric and EM noise levels have routinely be assessed in the field using the metal detector 'RD–8000 locating system' (RadioDetection Limited, UK).

### 2.4 Data Transformation

Quantitative interpretation of CINL–TEM soundings is often facilitated by transformation of the transient-decay response to apparent resistivity (Raiche, 1983). It effectively normalizes for the theoretical variations in the response due to any dependent survey parameter over a fairly homogeneous half-space. The transformation is also well-behaved over an uniform horizontally layered-earth. Moreover, apparent resistivity transform parameterizes the response in units of an intrinsic rock property. Therefore, it can be used to obtain a qualitative indication of the ground-resistivity distribution (Nabighian, 1979), or may be used as reasonable starting model in the layered-earth inversion (Goldmann et al., 1994).

Apparent resistivity is traditionally defined as the resistivity of a homogeneous half-space which will produce the same transient-decay response ($\partial h_z/\partial t)/I$, over a broad time range, as that measured over the real earth with the same survey parameters (Spies and Eggers, 1986). In other words, apparent resistivity is equal to the true ground resistivity only for the trivial case of a homogeneous half-space. If the ground is an uniform horizontally-layered earth, the apparent resistivity will vary with time in a distinctive manner, as is done for FDEM soundings over a broad frequency range. The late-time apparent resistivity formulation (Ward and Hohmann, 1988) is defined as

$$\rho_a = \frac{I^{2/3}\mu_0 a^{4/3}}{20^{2/3}\pi^{1/3}t^{5/3}}\left[\frac{-\partial h_z}{\partial t}\right]^{-2/3}.$$

Fig. 8 (lower) shows the typical NanoTEM late-time apparent resistivity curves computed for the stacked field transients, displayed on double-logarithmic axes, at the survey area. Because the definition of apparent resistivity is based mainly on the time behaviour of the signal at late-time when it decays as $t^{-5/2}$. For this reason, all curves are characterized by a descending branch at earliest-times (Fitterman and Stewart, 1986), where the apparent resistivity is higher than the half-space resistivity. In the intermediate- and late-time stages this formulation behaves similarly. There are other apparent resistivity formulations which avoid this problem in the early-time stage (e.g. Spies and Eggers, 1986). However, as long as the late-time apparent resistivity formulation is only applied to compare the stacked field transients from different CINL–TEM soundings and to visualize their forward modeling or inversion responses, there would be no problem anymore.

## 3. DC–RESISTIVITY (DCR) SOUNDING METHODS

### 3.1 Conceptual Background

In typical surface resistivity survey, artificially generated direct current (DC), or very low alternating current (AC) ($I$) are introduced into the ground using two current-electrodes ($C_A$, $C_B$) and the resulting potential differences ($\Delta V$) are measured between them using two potential-electrodes ($P_M$, $P_N$). Most commonly used four-electrode configurations are Schlumberger, Wenner, Lee, half-Schlumberger, dipole-dipole, pole-dipole, gradient and square arrays (Parasnis, 1997; Griffiths and King, 1981, Robinson and Courth, 1988; Telford et al., 1990; Keary and Brooks, 1991; Reynolds, 1997; Milsom, 2003).

Vertical electrical sounding (electrical drilling) (VES) survey is usually performed, using popularly either Schlumberger, Wenner or half-Schlumberger electrode configurations, at a fixed center point of the array, while the electrode spacings are progressively increased around it. This can image the resistivity variation with depth, reflecting a 1D horizontally-layered earth.

### 3.2 Depth-of-Investigation (DOI)

The depth-of-investigation for DCR methods is highly-controlled by the current-electrode half-spacing when conducting an electrical sounding survey (Roy and Apparao, 1971; Roy, 1972; Apparao, 1997; Oldenburg and Li, 1999). It is also dependent on how much DC–currents can be conveniently injected and how strong they can galvanically be distributed within an average ground resistivity. In practice, the effective depth-of-investigation is dependent not only on both the used electrode configuration geometry and the average ground resistivity and sampling time, but also on the overall signal-to-noise ratio (SNR), and hence the sensitivity and accuracy of the instrumentation. As a rule of thumb, the maximum current-electrode half-spacing should be, at least, three times the target depth-of-investigation for an electrical sounding survey.

### 3.3 ABEM™ Terrameter SAS–1000 Measuring System

The present DCR data were collected using the commercially available Terrameter SAS–1000 system (ABEM Instruments AB, Sweden) along 7 surveying traverses, comprising a total of 32 soundings (Fig. 3, lower).

Schlumberger vertical electrical soundings were employed with a maximum current-electrode half-spacing of 500 m. Identifying the sources-of-error is crucial in the scalar ABEM™ Terrameter SAS–1000 system (Fig. 2, right) because it has no real-time series. A procedure to get a rough error estimates is by repeating the measurements at every station few times to validate the data and rank the signal strength. These error estimates assess the background noise and can be representative throughout the rest of other stations. Additionally, measurements close to the both local sunrise and sunset timing are routinely avoided.

### 3.4 Data Transformation

The fundamental transformation equation for calculating ground apparent resistivity is given as

a

The array constant *K* is known as the geometrical factor (Parasnis, 1997) which depends on the relative distances between current and/or potential-electrodes.

The apparent resistivity for Schlumberger vertical electrical sounding survey is calculated as

$$\rho_a = \pi/a \times [(b/2)^2 - (a/2)^2] \times [\Delta V / I]$$

where *a* is the spacing between the potential-electrode pairs and *b* the half-spacing between two current-electrode pairs.

Measured data for vertical electrical sounding survey are customarily presented in the form of apparent resistivities ($\rho_a$) [Ohm.m] versus current-electrode half-spacings (AB/2) [m], displayed on double-logarithmic axes, for the progressive measurements (Fig. 9).

Raw data sets were extensively and consistently viewed, corrected, averaged and transformed using the very quick and easy-to-use plotting program CalcView–XL–1.0/05 (Farag, 2005). Final data sets were interpreted in terms of 1D/2D individual/joint-inverted smoothed-earth resistivity models using the software RES1DINV™–1.0/2009 and RES1DINV™–3.57/2010 (Geotomo Software, Malaysia), and JOINTEM©–1.4/2010 (Pirttijärvi, 2010). Topographic inputs and 1D/2D transformed or smoothed-earth resistivity models were contoured using the commercially available software package SURFER®–11.0/2012 (Golden Software, Inc., USA).

The DCR forward calculations and convolution computations are based originally on the algorithms of Koefoed (1979), Rijo (1970) and Sandberg (1990). While, the CINL–TEM forward calculations and convolution computations are based originally on the algorithms of Knight and Raiche (1982), Raiche and Spies (1981), Raiche (1984), Christensen (1990) and Sandberg (1990). The linearized inversion utilizes the adaptive-damping scheme in an iterative least-squares optimization fashion (Marquardt, 1963; Inman, 1975; Jupp and Vozoff, 1975; Petrick et. al., 1977; Lines and Treitel, 1984; Constable et. al., 1987; Loke and Barker, 1995, 1996a and 1996b; Pirttijärvi, 2003), trying to globally minimize an objective function in which the earth model is smoothly-descritized and the solution is regularized.

## 4. THE BEDOUIN VILLAGE 'FUKA'

### 4.1 Location, Accessibility and Importance

The Bedouin village 'Fuka' is located at the Northwestern Egyptian Mediterranean coast and roughly centered at latitude 31° 04' 30" N and longitude 27° 55' 45" E, covering an area of some 25 km$^2$. It is far about 225 km from Alexandria, about 65 km from Marsa Matrouh and about 475 km from Cairo. The village represents a part of the Fuka–Matrouh Mediterranean costal zone (Fig. 3, upper) which has been studied for a long time under the action of the 'Coastal Area Management Programme' in terms of 'Development of Mediterranean Tourism and Environment' (Klaric et al., 1999). It is among the most attractive development areas in Matrouh Governorate. This attraction is derived from the strategic water resources available in the village and relatively low population density, as well as the available natural potentials for near-future tourism. This can provide a growing interest for the village to become one of the most productive regions in Matrouh Governorate.

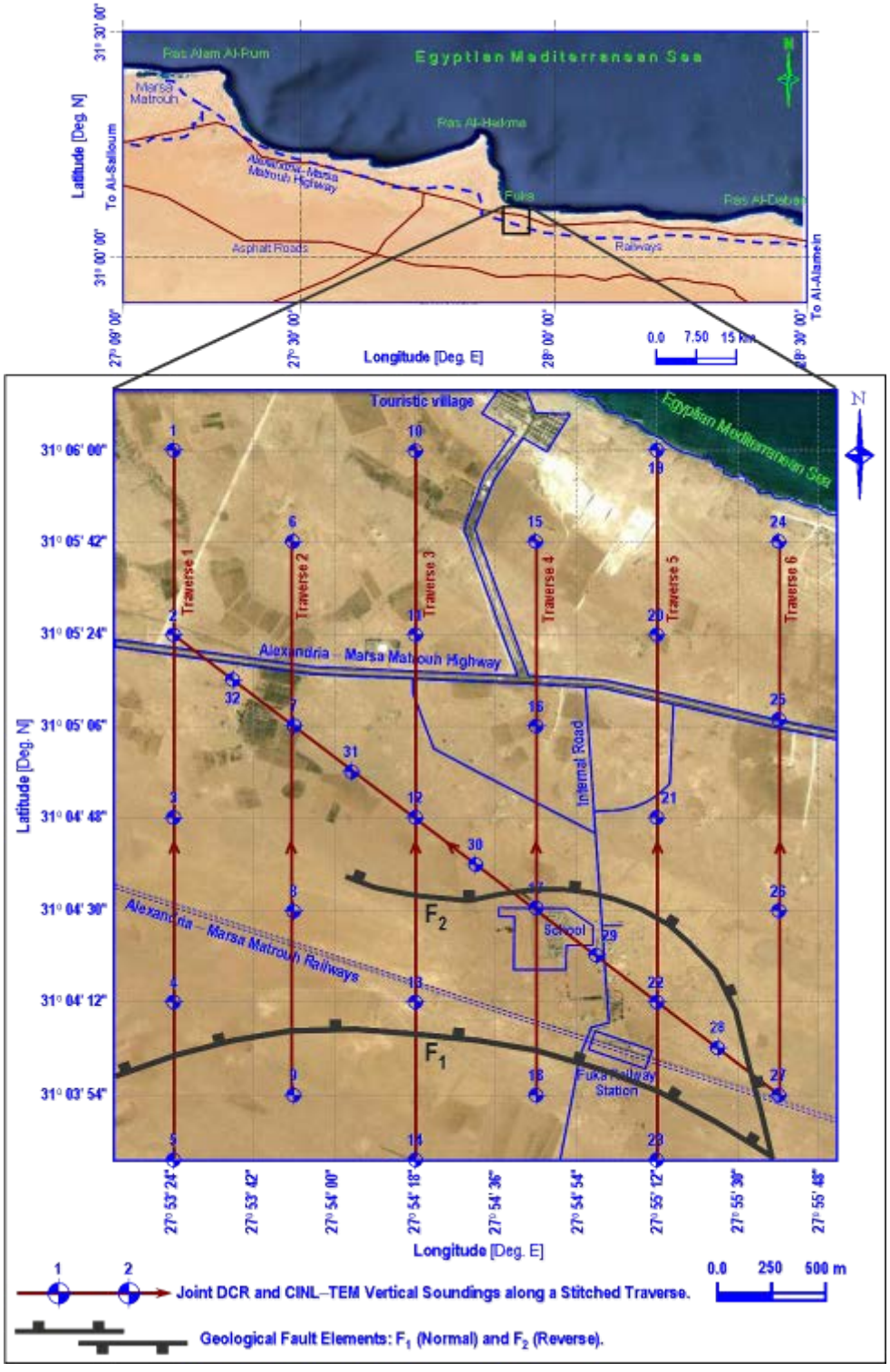


**Fig. (3): Satellite images showing (upper) the general position of the Fuka–Matrouh coastal zone at the Northwestern Egyptian Mediterranean and (lower) the locations of the jointly-conducted CINL–TEM and DCR vertical soundings along stitched traverses within the Bedouin village 'Fuka'.**

About 80% of the Bedouins, the main residents, in Fuka are traditionally involved in animal husbandry, sheep/goat herding, and cultivation of barely (Hordeum vulgare L.), vegetable and fruit trees. Cultivation of orchards predominates only southwestwards in deltas of wadies (Ayyad, 1995 and Shaltout and Ahmed, 2012). Fishing in the region is a minor activity. Additionally, about 15% depend on commerce as a source of income, where a double-line railway of fourth degree is already exist at the southern side of the village, which serves primarily for transportation of goods and water to far areas. The remaining 5% work in different jobs for the Matrouh Governorate and private sector.

### 4.2 Climate and Soil Conditions

The study area has semi-arid/arid Mediterranean climate (UNESCO, 1977). The summer season (May until September) is characterized by clear sunny sky and no rain. The winter season (October until March) is mainly windy. Most of the rainfall occurs in winter with maximum in December and January. The amount of rainfall in the study area is approximately 135 mm/year with certain variability (Griffiths, 1972 and Ali et al., 2007). The summer and winter monthly averages of air temperatures do not reach extreme values. The minimum monthly average of air temperature is reached in January about 8.0 °C, while the maximum monthly average is close to 29.5 °C in July. Relative humidity averages between 60% and 75% all year round. The prevailing wind is usually northwestern and strong in the winter season, blowing at a speed of about 22 km/hour in January. Otherwise, the wind speed decreases to about 15 to17 km/hour. Dry, warm dust-laden winds from the south/southwest, known as El-Khamasin storms, blow occasionally for about 45 days during spring and early summer (Shaltout and Ahmed, 2012).

Fuka's shoreline is characterized by a small bay with shallow, clear blue seawater. The soil is essentially alluvial (yellowish brown, stream water-based sandy loam with some of graded-grained gravel) of shallow nature, and therefore suitable for cultivation. It is classified, according to the potentials for reclamation, as of third to fourth grade. The beaches are composed mainly of white, well-polished, round, loose, Holocene/Recent carbonate sand with traces of shell fragments salts and silt. These loose sands, moving in the inland direction, gradually change to fairly-consolidated marine limestone forming small ridges that skirt the coast. Depressions close to the shoreline witness several sabkhas and salt marshes, and therefore unsuitable for cultivation.

### 4.3 Geomorphology and Geology

Regionally, the Fuka region represents a synclinal basin, within a great northeast–southwest monoclinal structure, and is covered by sedimentary rocks which belong to the Quaternary and Late Tertiary periods (Shata, 1955; Hassan and El-Ramly, 1966; El-Shamy et al., 1969; El-Fiky, 1996) (Fig. 4, upper). A geotraverse runs along the north–south direction crossing three distinct geomorphological units (Hammad, 1966; Shata, 1970; Swidan, 1978; Hassanein and El-Senussi, 1984); the coastal plain, the piedmont-like plain, and the structural plateau (Fig. 4, lower).

The coastal plain is an irregular narrow strip, running parallel to the Mediterranean Sea. Its maximum extent inland attains about 4.75 km. The northern part is marked by the occurrence of elongated Pleistocene oolitic limestone ridges (Alexandria Formation), running parallel to the present shoreline and alternating with shallow low-laying depressions of Quaternary alluvial deposits, sabkhas and salt marshes. The southern part is marked by the occurrence of scattered eroded, Middle Miocene marly/dolomitic limestone outcrops interbedded marly clay/clayey marl (Marmarica Formation), but sometimes it contains small sand sheets, dunes or hummocks. The topography is almost even, elevation differences within it don't exceeds 15.0 m. Further deeper in the village, a transitional zone is located between the coastal plain and the structural plateau contains a piedmont-like plain. Its width is laterally variable, changes from 1.0 to 13.75 km. This plain could be subdivided into depositional (aggraditional) and erosional (degradational) landforms marked by the development of Quaternary alluvial fans. The structural plateau consists of the southern tableland and its escarpment, having elevation ranges of about 110–145 and 90–100 m above sea level, respectively. It consists of fractured, cavernous/vuggy, fossiliferous Pliocene/Middle Miocene marly/dolomitic limestone with interbedded marly clay/clay (Marmarica and El-Hagif Formations).

### 4.4 Hydrogeology

The hydrogeological setting in Fuka basin is highly controlled by the relationship between its regional geomorphology, subsurface geological structures and climatic conditions. The regional rainfall and drained surface runoff, from the tableland and its escarpment (major watershed area), are directed to the north toward the piedmont-like and/or the coastal plains. They probably infiltrate into the near-surface Middle Miocene marly/dolomitic and/or Pleistocene oolitic limestone aquifers through interconnected joints, fractures, solution cavities/vuggs and pores. The elongated Pleistocene oolitic limestone ridges act as water divides where the rain and runoff waters seep along the slopes towards the bounding low-laying depressions which act as collecting water storage micro-basins (Atawa, 1979). Groundwater occurred in such local shallow aquifers, under both non-artesian and semi-perched conditions, figures a non-continuous watertable. The watertable depth is laterally-varied, ranged between few meters (at the northern/northwestern zones of the village) and more than 20 m (at the southeastern and middle zones of the village) from the existing natural ground surface. So, it is still as close as, or even below, the in-land regional sea level.

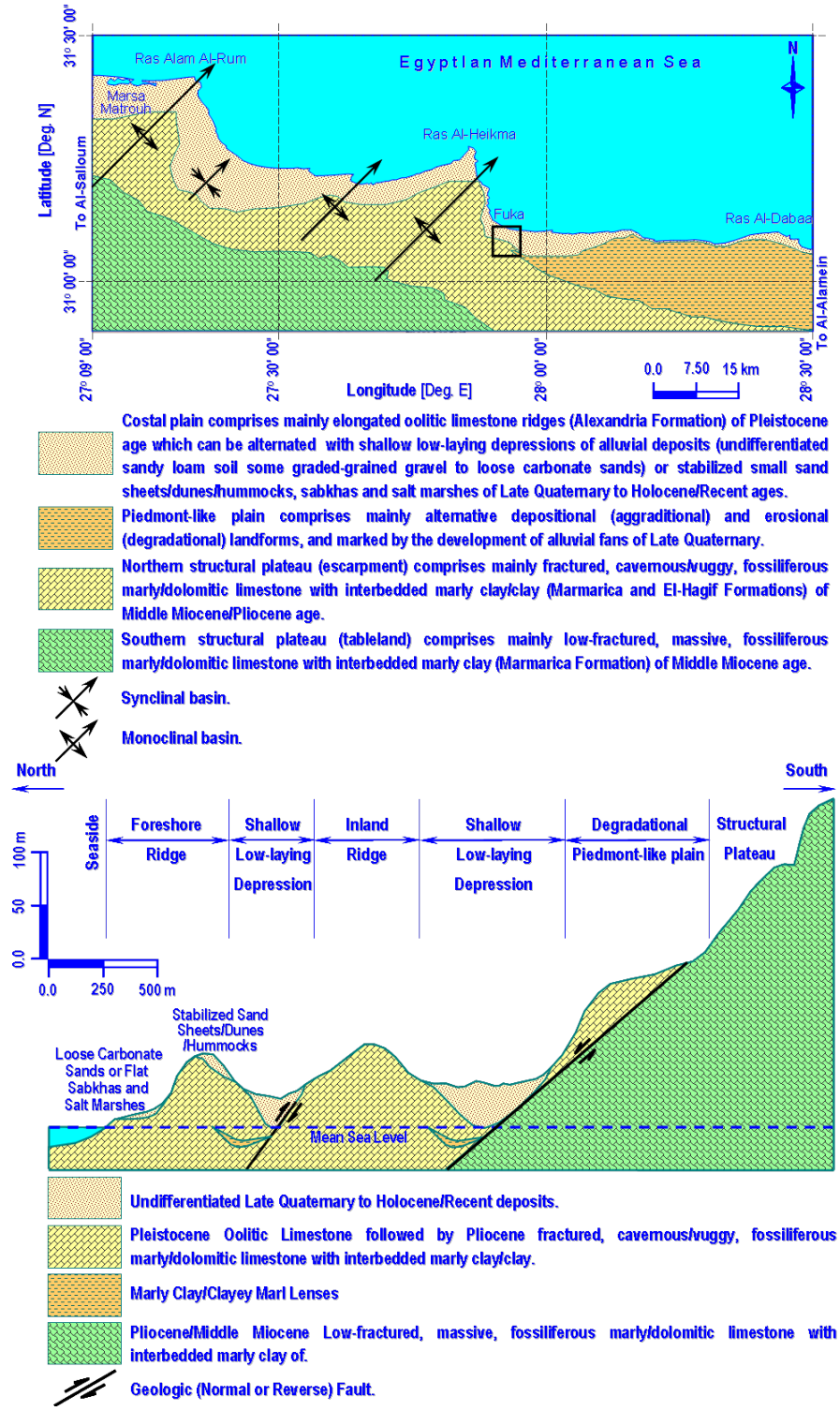


**Fig. (4): (Upper) A sketch map showing the whole geomorphological units (modified after El-Shamy et al., 1969; El-Fiky, 1996) and (lower) a regional geotraverse runs along the north–south direction crossing three distinct geomorphological units of the Fuka–Matrouh coastal zone at the Northwestern Egyptian Mediterranean.**

The marly clay/clayey marl lenses underneath the perched water-bearing limestones act as a thick subsurface confining base. The estimated annual perched water is close to 5.93 million $m^3$, about one-half of this quantity is unutilized annually.

The perched water quality varies widely and seasonally, but commonly can be classified as slightly-brackish/fairly fresh water (Eid, 1988 and Yousif and Bubenzer, 2012). Further deeper, the main fractured Middle Miocene marly/dolomitic limestone aquifer has a large quantity of highly-brackish/saline groundwater and is not usable. Yousif and Bubenzer (2012) stated that the total salinity of the deeper highly-brackish/saline groundwater can reach 9,800 mg/L.

A limited single pipeline (700 mm diameter) of treated potable water is provided from Alexandria and supplies only some urban centers along the Fuka–Matrouh Mediterranean costal zone (Ayyad, 1995). Therefore, the Bedouins in Fuka used to restore rainwater in the olden Roman reservoirs (Thaniya's). There are more than 37 Roman Thaniya's within the village, of which only one-half can be used.

## 5. Individual One-dimensional (1D) Smoothed-earth Inversion

The individual 1D smoothed-earth inversion of the measured CINL–TEM voltage and DCR apparent resistivity data at the survey area was carried out using a standard scheme of successive techniques. No a-priori information was initially introduced. The data were inverted using average-apparent-resistivity homogeneous half-spaces as starting models, in which the number of layers is so close to the number of time-windows or the number of electrode half-spacings. Their thicknesses were increased successively in the logarithmic-domain, set to the average effective depth-of-investigation and kept fixed during the inversion.

To drive a reasonable final layered-earth model, smoothed-earth inversion results were then blocked (or combined) such that a minimum structure is obtained. This least number of vertical layers is still well adapted to the intrinsic resolution capabilities of CINL–TEM or DCR data, and preservative to the general trend of the subsurface geology.

The individual inversion results from successive soundings, along each profile, were then stitched (assembled) to create resistivity sections in 2D (Fig. 5). These stitched sections were usually successful in determining any lateral resistivity variations present within the survey area. During all phases of the 1D individual inversion, one must make sure that the direct correlation to the subsurface geology was still reasonably maintained.

However, since the inductive CINL–TEM methods are only sensitive to the conductive subsurface media, the thicknesses of highly-resistive layers seem to be over-determined, and hence appeared somewhat too thick within the CINL–TEM resistivity sections in 2D (e.g., Rock Type C in Fig. 5, upper). While, since the galvanic DCR methods are only sensitive to the resistive subsurface media, the thicknesses of highly-conductive layers seem to be over-determined, and hence appeared somewhat too thick within the DCR resistivity sections in 2D (e.g., Rock Type E in Fig. 5, lower). Notably, the centers of such highly-resistive or highly-conductive layers are located reasonably.

## 6. Joint One-dimensional (1D) Smoothed-earth Inversion

### 6.1 Removal of Static Shift from DC–Resistivity Data

Near-surface, small-scale 3D resistivity inhomogeneities (or geologic interferences) may distort the encountered DCR electric field (Berdichevsky and Dmitriev, 1976; Larsen, 1977; Barker, 1981; Park, 1985; Sternberg et al., 1988; Bahr, 1991; Groom and Bahr 1992; Meju, 1996). The effect is known as DC–static shift and can ascend or descend the whole DCR apparent resistivity sounding curve by some scale factor. Since magnetic field is relatively unaffected by such galvanic distortions, a controlled-source magnetic field sounding data, such as CNL–TEM apparent resistivity sounding curve, can be used to identify and correct for DC–static shift. In this case, the DCR curve is shifted vertically, upward or downward, so that the sufficiently early/intermediate-time equivalent part of the CNL–TEM curve coincides with it.

To consistently correlate, compare and integrate both the CNL–TEM and DCR apparent resistivity sounding curves, displayed on the same double-logarithmic axes, a simple generic scaling relationship was suggested by Meju (2005) and empirically given as

$$L_{DCR} = \sqrt{\frac{2\,t\rho_a}{\pi\,\mu_o}},$$

where $L$ is the progressive current-electrode half-spacing [m] for the popular symmetric in-line four-electrode DCR (Schlumberger, Wenner, Lee and dipole-dipole) configurations.

The relationship between the observed DC–static shifted apparent resistivities ($\rho_S$), the correct apparent resistivities ($\rho_C$), and the constant static shift multiplier or scaling factor ($g$) at the sounding center may be given as $\rho_S = g\ \rho_C$ (Meju, 2005). Accurate data correlation requires a-priori information of $g$. Therefore, several trials have to be manually done to find an acceptable scaling factor for which the corrected DCR sounding curve matches well the CNL–TEM curve at a sufficiently early/intermediate-time equivalent part.

Most of the present DCR apparent resistivity curves showed a reasonable correlation degree with CNL–TEM curves, and hence don't exhibit substantial DC–static shifts (Fig. 6). Nevertheless, some limited DCR sounding data showed a certain degree-of-parallelism relative to the overlapping CNL–TEM apparent resistivity curves, and hence exhibit small vertical shifts to preferably be corrected (Fig. 7).

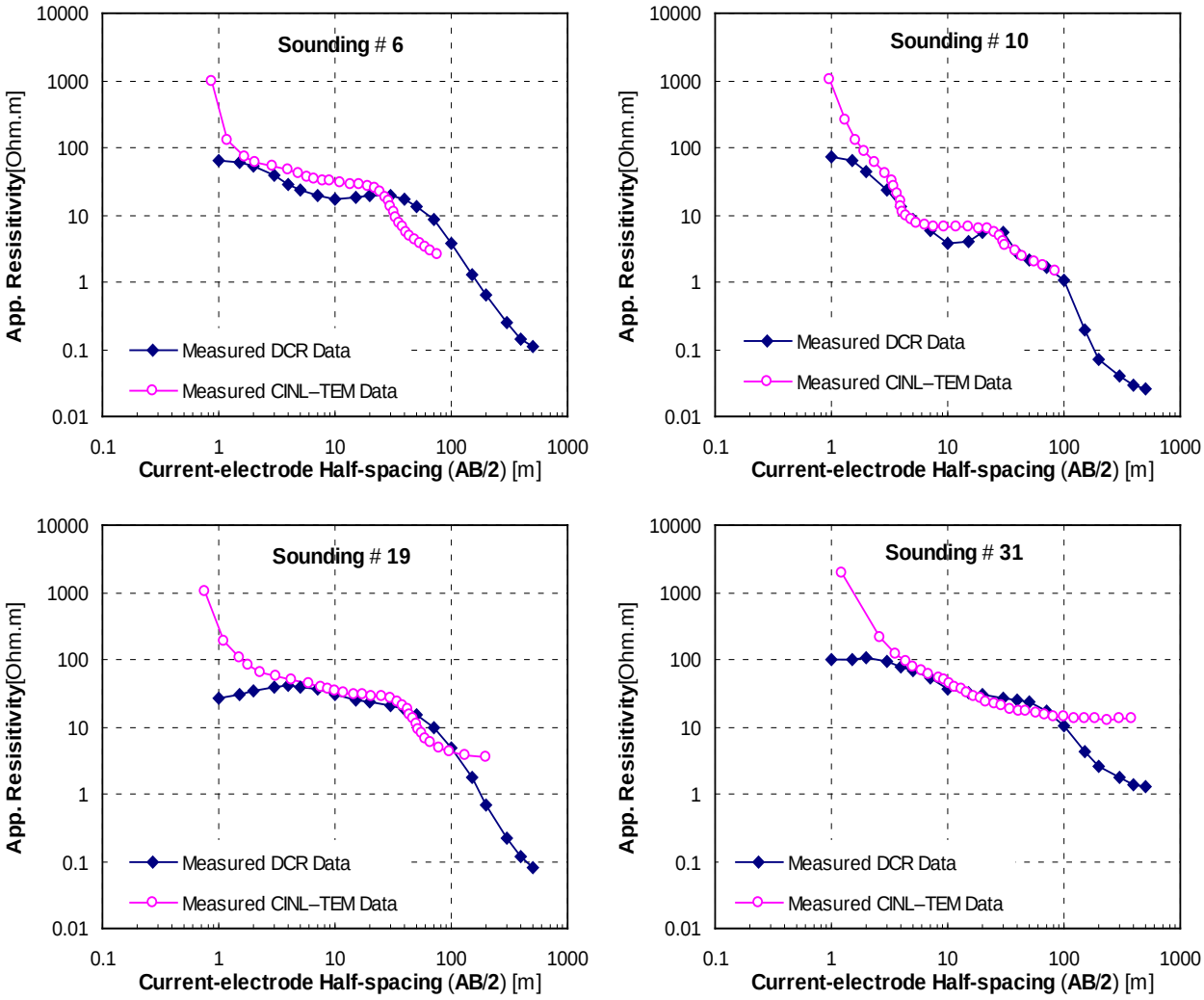


**Fig. (6): A suite of typical DCR apparent resistivity curves that showed a reasonable correlation degree with CNL–TEM response curves at the survey area, and hence don't exhibit substantial DC–static shifts.**

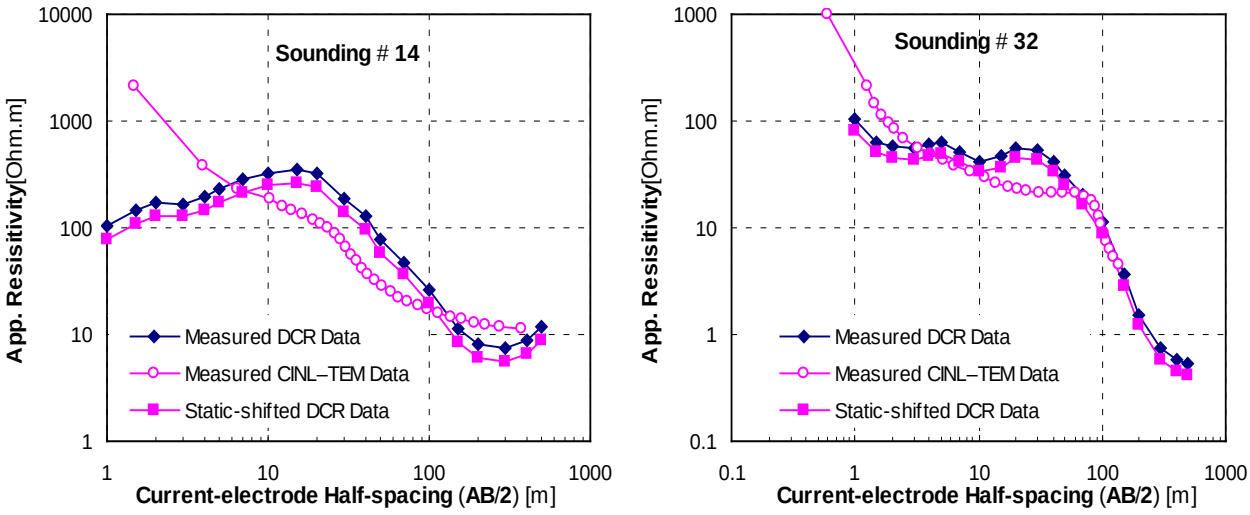


**Fig. (7): A suite of typical DCR apparent resistivity curves that showed a certain degree-of-parallelism relative to the overlapping CNL–TEM apparent resistivity curves, and hence exhibit small vertical shifts to preferably be corrected. The constant static shift multiplier or scaling factor (*g*) was ranged between 1.25 and 1.45.**

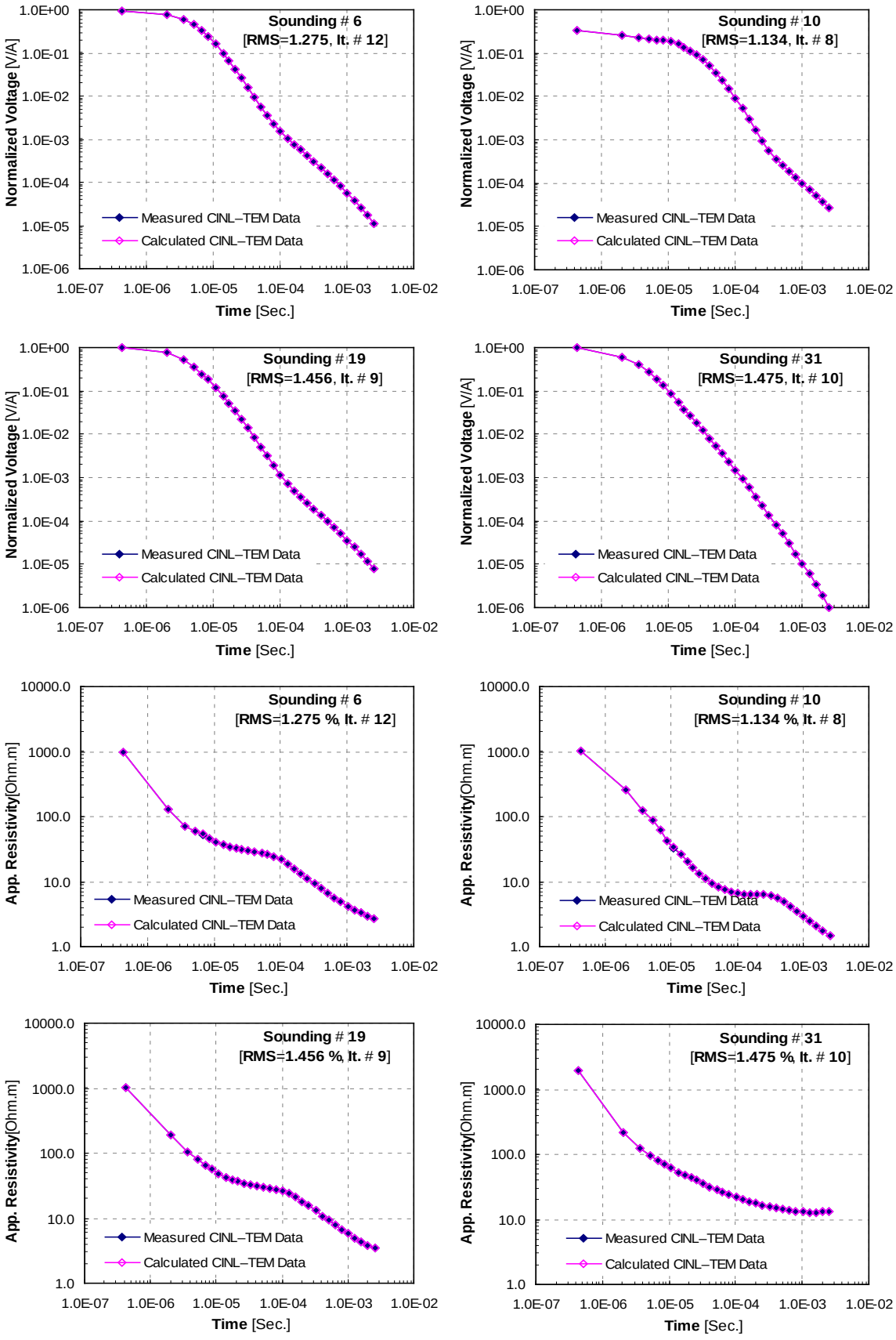


**Fig. (8): (Upper) A suite of typical measured–calculated transient-decay voltages and (lower) the corresponding late-time apparent resistivity curves, upon applying joint 1D smoothed-earth inversion, at the survey area. For better visualization the data are displayed without error bars.**

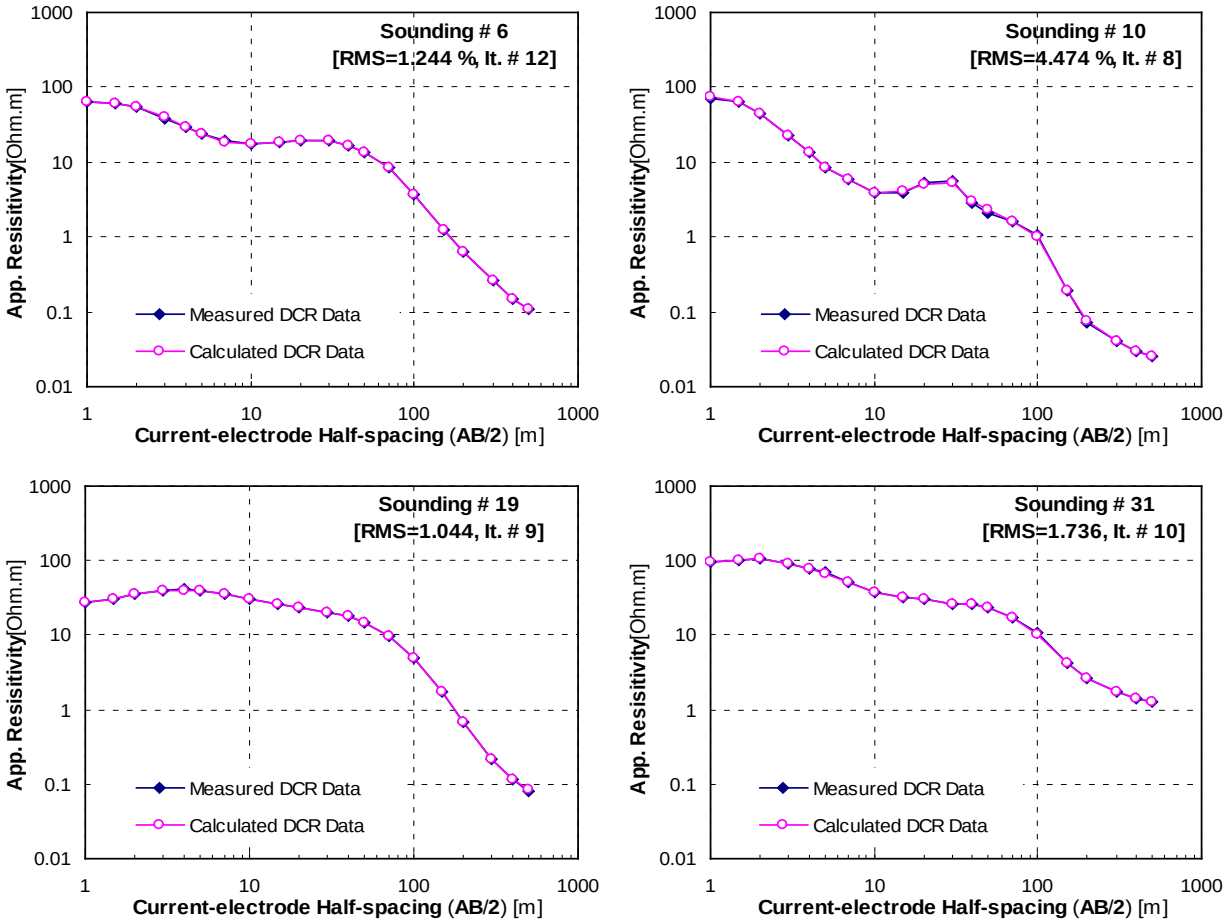


**Fig. (9): A suite of typical measured–calculated DCR apparent resistivity curves, upon applying joint 1D smoothed-earth inversion, at the survey area. For better visualization the data are displayed without error bars.**

## 6.2 Encountered Geoelectric Units

The encountered geoelectric units from the joint 1D smoothed-earth inversion have shown up, from top (youngest: Quaternary layers) to bottom (oldest: Middle Miocene layers) (Figs. 10 and 11), as follows:

1) A moderately/low-resistive surficial layer [Soil Type A] which represents the alluvial deposits, consisting of sandy loam soil with some graded-grained gravel (at the southeastern and middle zones of the village) to loose carbonate sands (at the northern/northwestern zones of the village). It is developed inland within the low-laying elongated depressions and drainage channels/terraces/fillings or foreshore within the small sand sheets/dunes/hummocks, and geologically belonging to the Late Quaternary to Holocene/Recent ages. Its base is probably composed of highly-weathered/fractured, weakly-cemented oolitic limestone/calcarenite. Thickness of this layer is laterally-varied, ranged from 0.25 to 4.75 m from the existing natural ground surface. Moist sabkhas and salt marshes close to the shoreline showed isolated surface conductivity highs.

2) A highly/moderately-resistive subsurface layer [Rock Type B] which represents both the fairly-consolidated oolitic limestone/calcarenite (at the southeastern, middle and northern/northwestern zones of the village) that is geologically belonging to the Pleistocene age and the marly/dolomitic limestone with interbedded marly clay/clay that is geologically belonging to the Middle Miocene age (at the southwestern zone of the village). Thickness of this layer is structurally-controlled, as it is originally forming the deep-seated coastal ridges, but generally ranged from 10.5 to 35.0 m. Due to the presence of interconnected joints, fractures, solution cavities/vuggs and pores, the lower part of these limestones [Rock Type C] is obviously highly-saturated with slightly/moderately-brackish perched water, having an intermediate/low electric resistivity.

3) A moderately/highly-conductive transitional layer [Rock Type D] which represents the relatively thick intercalations of marly clay/clayey marl and massive Middle Miocene marly/dolomitic or Pleistocene oolitic limestones. The upper part of this layer acts as a thick subsurface confining base for the overlaying perched water occurrences.

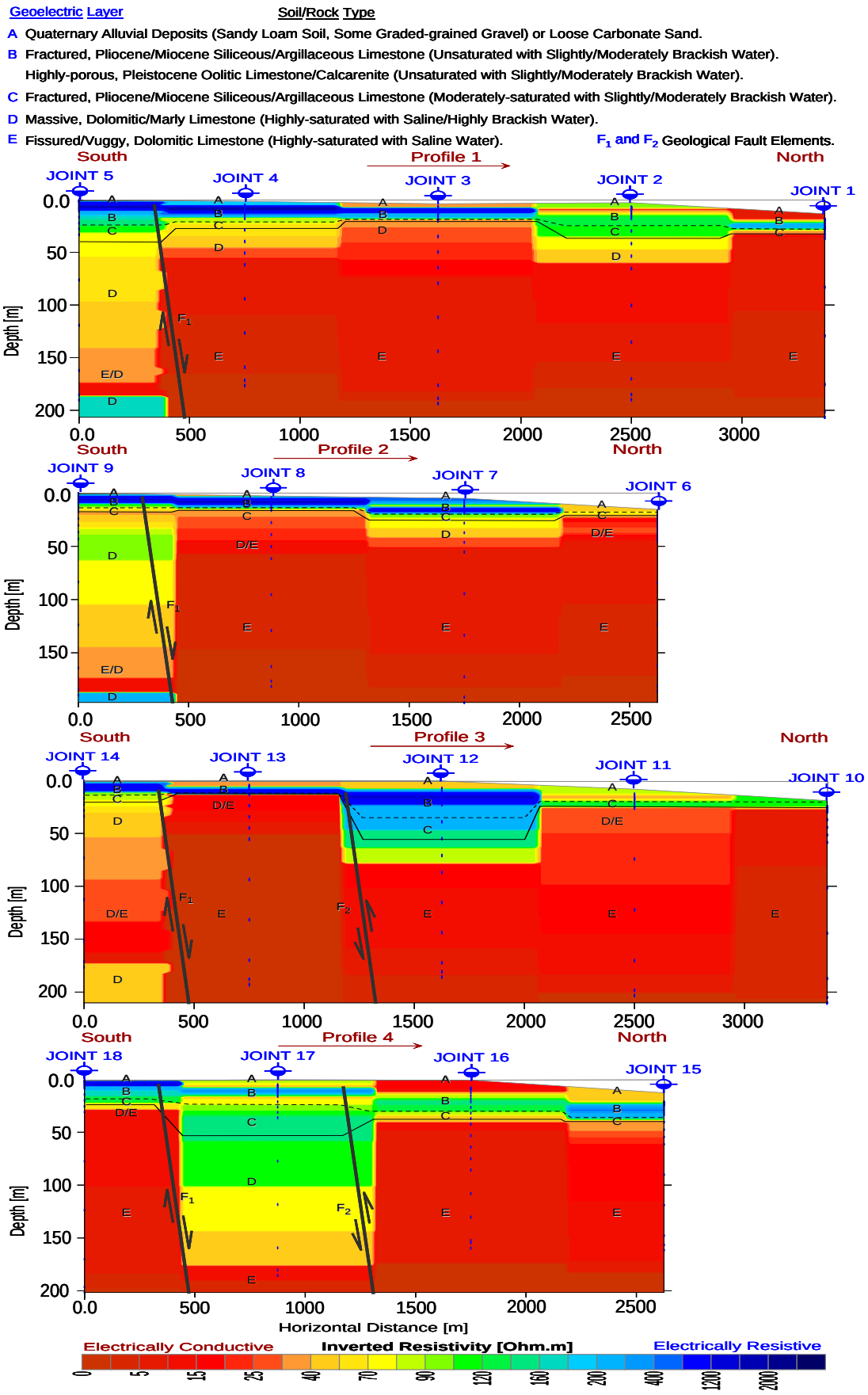


**Fig. (10): Stitched joint 1D smoothed-resistivity inverted sections in 2D below traverses 1 thru 4.**

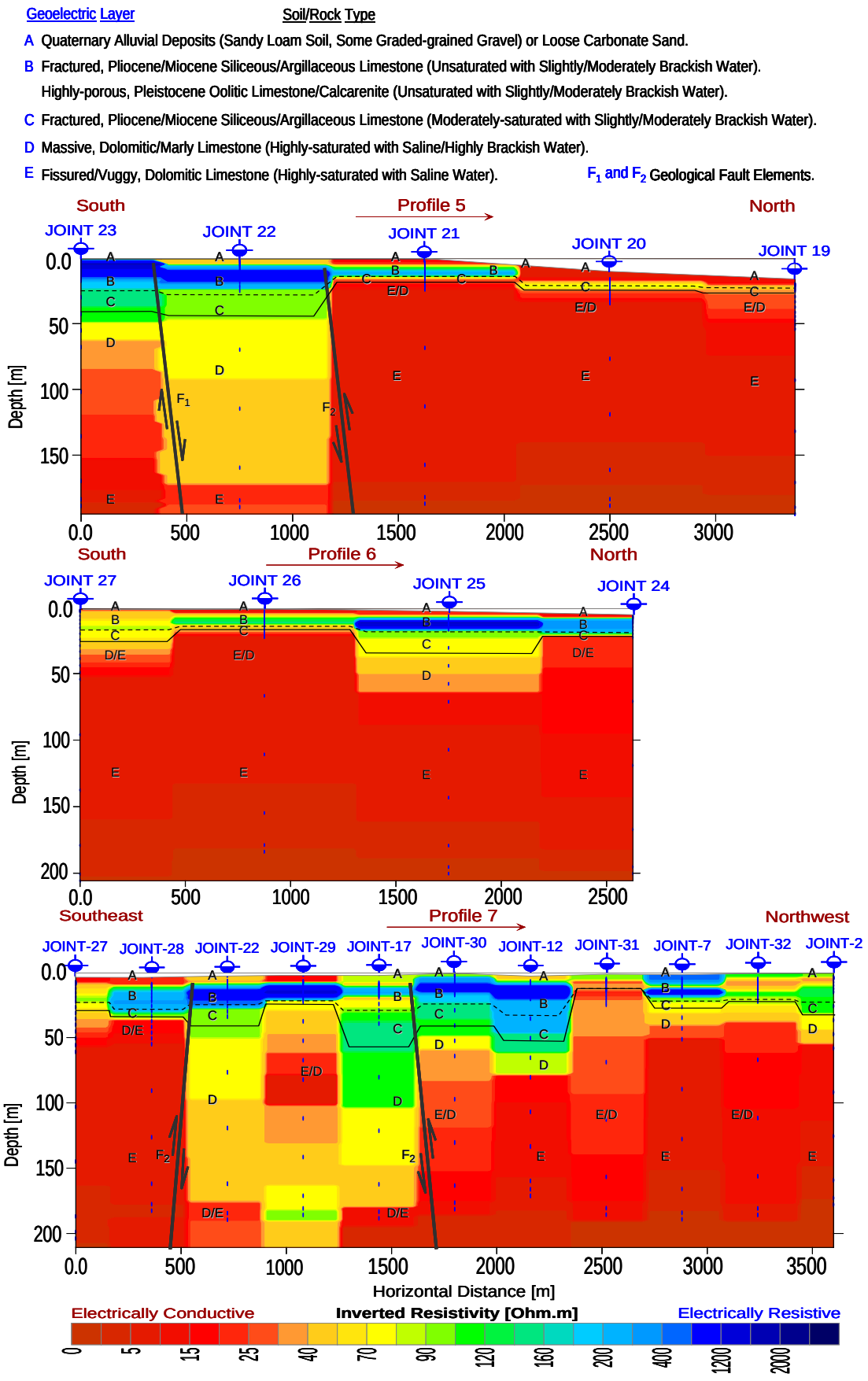


**Fig. (11): Stitched joint 1D smoothed-resistivity inverted sections in 2D below traverses 5 thru 7.**

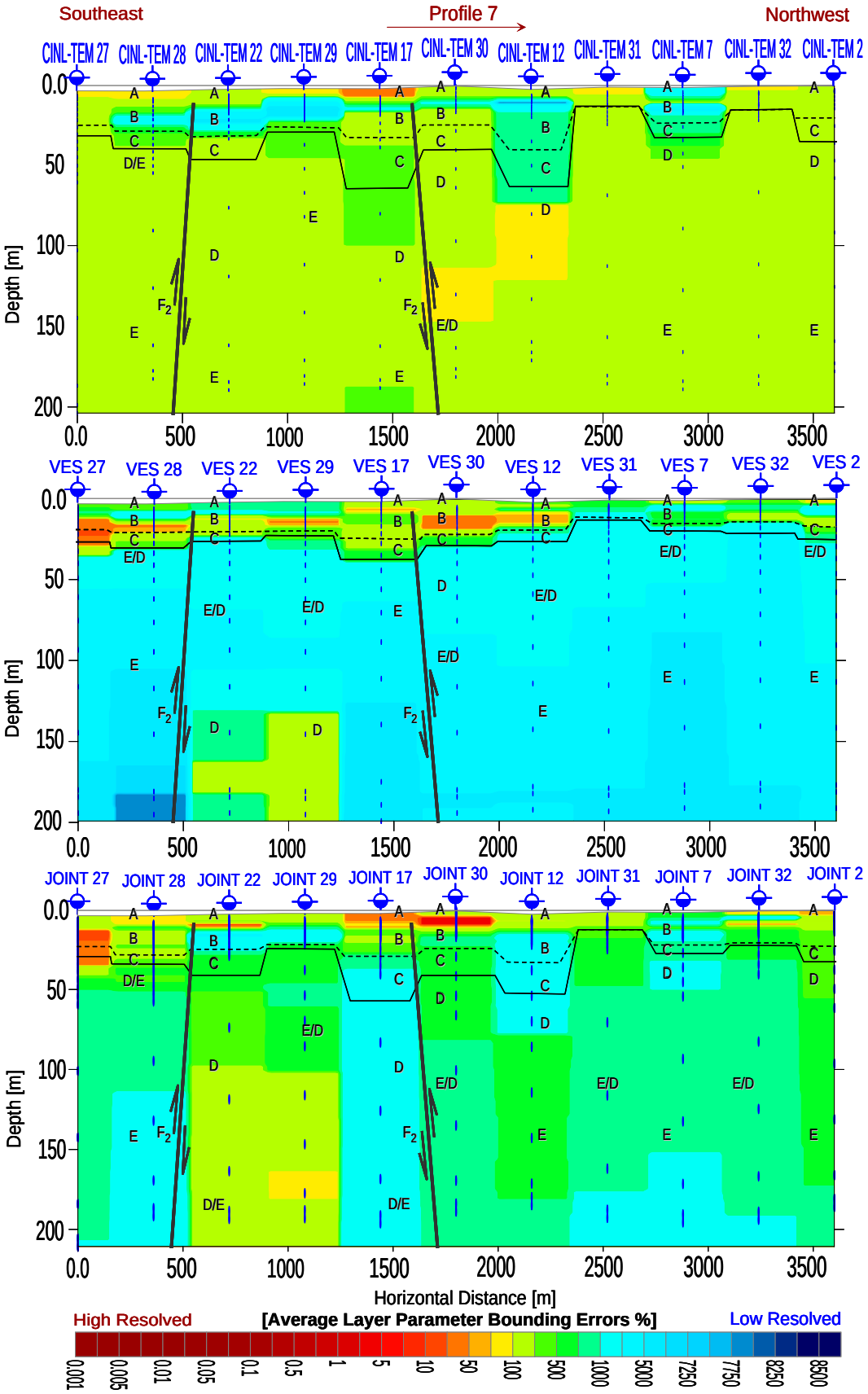


**Fig. (12): Stitched relative sensitivity (averaged layer bounding errors) sections in 2D below traverse 7, upon applying both the (upper & middle) individual and joint (lower) 1D smoothed-earth inversions.**

Thickness of this layer is structurally-controlled, as it is originally forming the deep-seated synclinal basin, within a regional northeast–southwest monocline and local geological fault element $F_1$ (abrupt lateral resistivity changes due to normal faulting) and $F_2$ (abrupt lateral resistivity changes due to reverse faulting).

Such deep structural fashion confined several fractured, cavernous and vuggy Middle Miocene limestone beds, containing large amount of brackish/saline water [Rock Type E]. The prevailing highly-saline nature close to the shoreline could also be delineated, where several extremely-high conductive deep zones were imaged.

4) The shallow slightly/moderately-brackish perched water, intermediate/deep brackish/highly-saline water and extremely/hyper-saline seawater are fundamentally interrelated. The vertical bounding interface within the village varies from 6.0 m (at the upper middle and northern/northwestern zones) to 20.0 m (at the southeastern and lower middle zones). The hydrologic relation between such water types is controlled by the well-known principle of the saltwater intrusion into coastal aquifers.

The final inversion results fit the measured data within 0.975 to 4.474 RMS % (Figs. 8 and 9). Importantly, a significant resolution improvement for both the shallow and deep resistivity structures has been achieved when inverting both data sets jointly. The layer bounding errors for both the jointly-inverted CINL–TEM highly-resistive and DCR highly-conductive layers were impressively decreased (Fig. 12).

## 7. CONCLUDING REMARKS

The present field survey highlighted the applicability, efficiency and reliability of utilizing both the CINL–TEM and DCR sounding methods, than any individual use, for better imaging and differentiating the strategic shallow perched water-bearing layers from the whole intermediate/deep groundwater occurrences along the Northwestern Mediterranean coastal plain of Egypt.

Finally, to gain a physically reasonable earth model, it is therefore necessary to carefully inspect the inversion statistics. The inversion statistics and its standard resolution/sensitivity analysis (e.g., linear equivalence analysis) are just as important as the inversion itself. The inverted model parameters (layer thicknesses or electrical resistivities) are only well-resolved by field measurements, and therefore have large contributions (or relative importance) on calculated data during the inversion and can reliably be determined, if their layer bounding errors were found as small as possible. Whereas, model parameters are only bad-resolved by field measurements, and therefore have small contributions (or relative importance) on calculated data during the inversion and can ambiguously be determined, if their layer bounding errors were found larger.

## 8. ACKNOWLEDGMENT

This work was funded by the Center for Special Studies and Programs (CSSP), Bibliotheca Alexandrina (BA), Alexandrina, Egypt [Research Grants–Earth Sciences–Contract No. 070140–BA/CSSP–07/08]. We would like to thank Prof. Dr. Salah El-Deen A. Mousa [Geophysics Department, Faculty of Science, Ain Shams University, Cairo, Egypt] who has introduced the Bedouin village 'Fuka' to us and interestingly declared the importance of its available strategic perched water occurrences. CINL–TEM, DCR and EM metal detector measuring systems were kindly provided from both the 'Geophysics Department, Faculty of Science, Ain Shams University, Cairo, Egypt' and 'Helal Group for Geotechnical–Geological–Geophysical (3G) Services, Cairo, Egypt' [a private consulting firm operating in Egypt and Arabian countries], during all phases of field measurements. We are indebted to them therefore. The discussion about the DC–static shift with Prof. Dr. Sultan A. S. Araffa [National Research Institute of Astronomy and Geophysics (NRIAG), Helwan, Cairo, Egypt] was more than useful.

## 9. REFERENCES

**Albouy, Y., Andrieux, P., Rakotondrasoa, G., Ritz, M., Descloitres, M., Join, J-L. and Rasolomanana, E., 2001**. Mapping Coastal Aquifers by Joint Inversion of DC and TEM Soundings – Three Case Histories. Ground Water, 39, 87–97.

**Ali, A.O., Rashid, M., El-Naggar, S., Abdul Al, A., 2007**. Water harvesting options in the drylands at different spatial scales. Land Use Water Resour. Res., 7, 1–13.

**Apparao, A., 1997**. Developments in geoelectrical methods. Oxford & IBH Publishing Co., New Delhi.

**Atawa, S.M.M., 1979**. Hydrogeology and Hydrogeochemistry of the Northwestern Coast of Egypt. Ph.D. Thesis, Geology Department, Faculty of Science, Alexandria University, Egypt.

**Ayyad, M.A., 1995**. A contribution to Fuka–Matrouh coastal area management programme: A framework for accumulating consequential data and knowledge. Split, Blue Plan/Regional Activity Centre (BP/RAC), United Nations Environment Programme (UNEP).

**Bahr, K., 1991**. Geological noise in magnetotelluric data: a classification of distortion types. Physics of the Earth and Planetary Interiors, 60, 24–38.

**Barker R.D., 1981**. The offset system of electrical resistivity and its use with a multicore cable. Geophysical Prospecting, 29, 12–143.

**Berdichevsky, M.N. and Dmitriev, V.I., 1976**. Distortion of magnetic and electrical fields by surface lateral inhomogeneities. Acta Geodaetica, Geophysica et Montanista, Academy of Science of Hungary, 11, 447–483.

**Christensen, N.B., 1990**. Optimized fast Hankel transform filters. Geophysical Prospecting, 38, 545–568.

**Constable, S.C., Parker, R.L. and Constable, C.G., 1987**. Occam's Inversion: A practical algorithm for generating smooth models from EM sounding data. Geophysics, 52, 289–300.

**Eid, Y.M., 1988**. The general ourism development plan for Ras El-Hekma tourist area. Unpublished Internal Research Project Report, Egyptian Ministry of Tourism.

**El-Fiky, A.A., 1996**. Geophysical and hydrogeological investigations on some groundwater problems at the area between Fuka and Ras Umm El-Rakham, Mediterranean coastal zone, Egypt. Ph.D. Thesis, Geology Department, Faculty of Science, Alexandria University, Egypt.

**El-Shamy, I.Z., El-Shazly, M.M. and Shata, A.A. 1969**. Contribution to the geology of El-Dabaa area, western Mediterranean littoral zone (Part I): Geomorphology and morphology. Bull. Inst. Désert d'Egypte, 19(1), 63–96.

**Farag, K.S.I., 2005**. Multi-dimensional Resistivity Models of the Shallow Coal Seams at the Opencast Mine 'Garzweiler I' (Northwest of Cologne) inferred from Radiomagnetotelluric, Transient Electromagnetic and Laboratory Data. Doktorarbeit, Institut für Geophysik und Meteorologie, Universität zu Köln, Cologne, Germany.

**Fitterman, D.V. and Stewart, M.T., 1986**. Transient electromagnetic sounding for groundwater. Geophysics, 51, 995–1055.

**Goldman, M., du Plooy, A. and Eckard, M., 1994a**. On reducing ambiguity in the interpretation of transient electromagnetic sounding data. Geophysical Prospecting, 42, 3–25.

**Griffiths, D.H. and King, R.F., 1981**. Applied Geophysics for Geologists and Engineers. Pergamon Press, Oxford.

**Griffiths, J.F., 1972**. Climate of Africa. In: World Survey of Climatology, 10. Elsevier, Amsterdam.

**Groom, R.W. and Bahr, K., 1992**. Corrections for near surface effects: Decomposition of the magnetotelluric impedance tensor and scaling corrections for regional resistivities: A tutorial. Survey in Geophysics, 13, 341–379.

**Hammad, F.A., 1966**. The geology of water supplies in Ras El-Hekma area, western Mediterranean coastal zone, Egypt. M.Sc. Thesis, Geology Department, Faculty of Science, Cairo University, Egypt.

**Hassan, A.A. and El-Ramly, I.M., 1966**. Preliminary groundwater investigation in Ras El-Hekma area, western Mediterranean littoral, U.A.R. Special Report submitted to the Bull. Inst. Désert d'Egypte, Cairo.

**Hassanein, A.M. and El-Senussi, M.Y., 1984**. Geomorphology aspects of the area between longitudes 26° 30' and 27° 30' E along the Mediterranean coast zone, Egypt. Bull. Fac. Sci., Zagazig Univ., Zagazig, 6, 136–155.

**Helwig, S.L., Bergers, R. and Koch, O., 2004**. Entwicklung einer Drei-Komponenten-Empfangsspule für oberflächennahe TEM-Messungen. In: Protokoll über die 64. Jahrestagung der Deutschen Geophysikalischen Gesellschaft, Berlin, DGG, EMP10.

**Hohmann, G.W. and A.P. Raiche., 1988**. Inversion of controlled-source electromagnetic data. In: **Nabighian, M.N.** (Ed.), Electromagnetic Methods in Applied Geophysics, Vol. 1: Theory, Society of Exploration Geophysicists, Tulsa, 469–503.

**Inman, J.R., 1975**. Resistivity inversion with ridge regression. Geophysics, 40, 798–817.

**Jackson, D.D., 1972**. Interpretation of inaccurate, insufficient, and inconsistent data. Geophys. J. Roy. Astr. Soc., 28, 97–109.

**Jupp, D.L.B. and Vozoff, K., 1975**. Stable iterative methods for the inversion of Geophysical data. Geophys. J. Roy. Astr. Soc., 42, 957–976.

**Keary, Ph. and Brooks, M., 1991**. An Introduction to Geophysical Exploration, Second Edition. Blackwell Scientific Publications, Oxford.

**Klaric, Z., Komilis, P., Dragicevic, M., Berlengi, G. and Surucu, F., 1999**. Carrying Capacity Assessment for Tourism Development of the Coastal Area Management Programme (CAMP) Fuka–Matrouh, Egypt. Split, Priority Actions Programme/Regional Activity Centre (PAP/RAC), United Nations Environment Programme (UNEP).

**Knight, J.H. and Raiche, A.P., 1982**. Transient electromagnetic calculations using the Gaver–Stehfest inverse Laplace transform method. Geophysics, 44, 47–50.

**Koefoed, O., 1979**. Geosounding Principles, 1. Resistivity Sounding Measurements. Elsevier Scientific Publishing, Amsterdam.

**Larsen, J.C., 1977**. Removal of local surface conductivity effects from low frequency mantle response curves. Acta Geodaetica, Geophysica et Montanista, Academy of Science of Hungary, 12, 183-186.

**Lines L.R. and Treitel S., 1984**. Tutorial: A review of least-squares inversion and its application to geophysical problems. Geophysical Prospecting, 32, 159–186.

**Loke, M.H. and Barker, R.D., 1995**. Least-squares deconvolution of apparent resistivity pseudosections. Geophysics, 60, 1683–1690.

**Loke, M.H. and Barker, R.D., 1996a**. Practical techniques for resistivity surveys and data inversion. Geophysical Prospecting, 44, 499–523.

**Loke, M.H. and Barker, R.D., 1996b**. Rapid least-squares inversion of apparent resistivity pseudo sections by a quasi-Newton method. Geophysical Prospecting, 44, 131–152.

Marquardt, D. W., 1963. An algorithm for least-squares estimation of non-linear parameters. SIAM J., 11(2), 431–441.

**Meju M.A., 1994**. Geophysical Data Analysis: Understanding Inverse Problem–Theory and Practice. Society of Exploration Geophysicists (SEG) Course Notes Series, 6, SEG Publishers, Tulsa, Oklahoma.

**Meju, M.A., 1996**. Joint inversion of TEM and distorted MT soundings: Some effective practical considerations. Geophysics, 61, 56–65.

**Meju M.A., 2005**. Simple relative space–time scaling of electrical and electromagnetic depth sounding arrays: implications for electrical static shift removal and joint DC-TEM data inversion with the most-squares criterion. Geophysical Prospecting, 53, 463–479.

**Milsom, J., 2003**. Field Geophysics, Third Edition. The Geological Field Guide Series. John Wiley and Sons Ltd., London, West Sussex.

**Nabighian, M.N. and Macnae, J.C., 1991**. Time-domain electromagnetic prospecting methods. In: **Nabighian, M.N.** (Ed.), Electromagnetic Methods in Applied Geophysics, Vol. 2A, Society of Exploration Geophysicists, Tulsa, 427–520.

**Nabighian, M.N., 1979**. Quasi-static transient response of a conducting half-space an approximate representation. Geophysics, 44, 1700–1705.

**Oldenburg, D.W. and Li,Y., 1999**. Estimating depth of investigation in DC resistivity and IP surveys. Geophysics, 64, 403–416.

**Oristaglio, M.L. and Hohmann, G.W., 1984**. Diffusion of electromagnetic fields into two-dimensional earth. Geophysics, 49, 870–894.

**Paal, G., 1965**. Ore prospecting based on VLF-radio signals. Geoexploration, 3, 139–147.

Parasnis, D. S., 1997. Principles of Applied Geophysics. Fifth Edition. Chapman and Hall, London.

**Park, S. K., 1985**. Distortion of magnetotelluric sounding curves by three-dimensional structures. Geophysics, 50, 786–797.

**Petrick, W.R., Pelton, W.H. and Ward, S.H., 1977**. Ridge regression inversion applied to crustal resistivity sounding data from South Africa. Geophysics, 42, 995–1006.

**Pirttijärvi, M., 2003**. Numerical modeling and inversion of geophysical electromagnetic measurements using a thin plate model. Ph.D. Thesis, University of Oulu, Department of Geosciences, Division of Geophysics, Oulu, Finland.

**Pirttijärvi, M., 2010**. Joint interpretation of electromagnetic and geoelectrical soundings using 1-D layered earth model: User's Guide to the JOINTEM Program Version–1.4, University of Oulu, Department of Geosciences, Division of Geophysics, Oulu, Finland.

**Raiche, A.P., 1983**. Comparison of apparent resistivity functions for transient electromagnetic methods. Geophysics, 48, 787–789.

**Raiche, A.P. and Spies, B.R., 1981**. Coincident loop transient electromagnetic master curves for interpretation of two-layer earths. Geophysics, 46, 53–64.

**Raiche, A.P., 1984**. The effect of ramp function turn-off on the TEM response of layered earth. Exploration Geophysics, 15, 37–41.

**Raiche, A.P., Jupp, D.L.B. and Vozoff, K., 1985**. The joint use of coincident loop transient electromagnetic and Schlumberger sounding to resolve resistive layers. Geophysics, 50, 1618–1627.

**Reynolds, J. M., 1997**. An Introduction to Applied and Environmental Geophysics. John Wiley and Sons Ltd., New York.

**Rijo, L., 1970**. Modeling of electric and electromagnetic data. Ph.D. Thesis, University of Utah, Salt Lake, Utah, USA.

**Robinson, E.S., and Courth, C., 1988**. Basic Exploration Geophysics, Cambridge University Press.

**Roy, A. and Apparao, A., 1971**. Depth of investigations in direct current resistivity prospecting. Geophysics, 36, 943–959.

**Roy, A., 1972**. Depth of investigations in Wenner, three-electrode and dipole-dipole DC resistivity methods. Geophysical Prospecting, 20, 329–340.

**Sandberg, S.K., 1990**. Microcomputer software for individual or simultaneous inverse modeling of transient electromagnetic, resistivity and induced polarization soundings. Open-file Technical Report OFT 90–1, New Jersey Geological Survey, Trenton, New Jersey, USA.

**Sandberg, S.K., 1993**. Examples of resolution improvement in geoelectrical soundings applied to groundwater investigations. Geophysical Prospecting, 41(8), 207–227.

**Shaltout, K. and Ahmed, D.A., 2012**. Ecosystem Services of the Flora of Southern Mediterranean Desert of Egypt. Ethnobotany Research and Applications, 10, 403–422.

**Shata, A. 1955**. An introductory note on the geology of the northern portion of the Western Desert of Egypt. Bull. Inst. Désert d'Egypte, 2, 96–106.

**Shata, A., 1970**. The geomorphology, pedology and hydrogeology of the Mediterranean coastal desert of U.A.R. Symposium on the Geology of Libya, Tripoli, 431–446.

**Spies, B.R. and Eggers, D.E., 1986**. The use and misuse of apparent resistivity in electromagnetic methods. Geophysics, 51, 1462–1471.

**Spies, B.R., 1989**. Depth of investigation in electromagnetic sounding methods. Geophysics, 54, 872–888.

**Sternberg, B. K., Washburne, J. C. and Pellerin, L., 1988**. Correction for the static shift in magnetotellurics using transient electromagnetic soundings. Geophysics, 53, 1459–1468.

**Swidan, A.S., 1978**. Water budget analysis for the northwestern coastal zone of the Arab Republic of Egypt. Ph.D. Thesis, Geology Department, Faculty of Science, Cairo University, Egypt.

Telford, W. M., Geldart, L. P., and Sheriff, R. E., 1990. Applied Geophysics, Second Edition. Cambridge University Press, Cambridge.

**UNESCO (United Nations Educational, Scientific and Cultural Organization), 1977**. Map of the World Distribution of Arid Regions. MAB Technical Notes, 7.

**Ward, S.H. and Hohmann, G.W., 1988**. Electromagnetic theory for Geophysical applications. In: Nabighian, M. N. (Ed.), Electromagnetic Methods in Applied Geophysics, Vol. 1, Society of Exploration Geophysicists, Tulsa, 131–250.

**West, G.F. and Macnae, J.C., 1991**. Physics of the electromagnetic induction exploration method. In: Nabighian, M. N. (Ed.), Electromagnetic Methods in Applied Geophysics, Vol. 2A, Society of Exploration Geophysicists, Tulsa, 5–45.

**Yousif, M. and Bubenzer, O., 2012**. Perched groundwater at the northwestern coast of Egypt: A case study of the Fuka Basin. Appl. Water Sci., 2, 15–28.

**Zonge Engineering and Research Organization Inc., 2000**. Zonge GDP–32II Multifunction Receiver Operation Manual. Zonge Engineering and Research Organization Inc., Tucson, Arizona.